Microcluster colloidosomes for hemostat delivery into complex wounds: A platform inspired by the attack action of torpedoes

Bitao Lu [a], Enling Hu [a,b], Ruiqi Xie [a,b], Kun Yu [a,b], Fei Lu [a,b], Rong Bao [c], Chenhui Wang [d], Guangqian Lan [a,b,*], Fangyin Dai [a,b,**]

[a] State Key Laboratory of Silkworm Genome Biology, College of Sericulture, Textile and Biomass Sciences, Southwest University, Chongqing, 400715, China
[b] Chongqing Engineering Research Center of Biomaterial Fiber and Modern Textile, Chongqing, 400715, China
[c] The Ninth People's Hospital of Chongqing No. 69 Jialing Village, BeiBei District, Chongqing, 400715, China
[d] Chongqing Key Laboratory of Natural Product Synthesis and Drug Research, School of Pharmaceutical Sciences, Chongqing University, 55 South Daxuecheng Road, Chongqing, 401331, China

A B S T R A C T

Complex yet lethal wounds with uncontrollable bleeding hinder conventional hemostats from clotting blood at the source or deep sites of injury vasculature, thereby causing massive blood loss and significantly increased mortality. Inspired by the attack action of torpedoes, we synthesized microcluster (MC) colloidosomes equipped with magnetic-mediated navigation and "blast" systems to deliver hemostats into the cavity of vase-type wounds. $CaCO_3/Fe_2O_3$ (CF) microparticles functionalized with Arg-Gly-Asp (RGD) modified polyelectrolyte multilayers were co-assembled with oppositely charged zwitterionic carbon dots (CDs) to form MC colloidosomes, which were loaded with thrombin and protonated tranexamic acid ($TXA-NH_3^+$). The composite microparticles moved against blood flow under magnetic mediation and simultaneously disassembled for the burst release of thrombin stimulated by $TXA-NH_3^+$. The CO_2 bubbles generated during disassembly produced a "blast" that propelled thrombin into the wound cavity. Severe bleeding in a vase-type hemorrhage model in the rabbit liver was rapidly controlled within ~60 s. Furthermore, *in vivo* subcutaneous muscle and liver implantation models demonstrated excellent biodegradability of MC colloidosomes. This study is the first to propose a novel strategy based on the principle of torpedoes for transporting hemostats into vase-type wounds to achieve rapid hemostasis, creating a new paradigm for combating trauma treatment.

1. Introduction

Complex and lethal wounds with acute massive bleeding are the chief cause of traumatic deaths in battlefield settings [1]. Nearly 25% of the 4596 battlefield fatalities are largely related to uncontrolled bleeding [2]. More than 50% of these deaths can be avoided if appropriate hemostatic materials are applied within the initial hour [3]. However, currently available hemostatic materials involving sponge-like chitosan dressing [4], modified chitosan powder [5], oxidized cellulose [6] and zeolite powder [7] can only cater to superficial, externally accessible, and compressible wounds and display low efficiency for severe trauma generated by small-caliber firearms or improvised explosive devices [8]. This is mainly because these hemostatic materials only accelerate the coagulation of supernatant blood on the wound surface and are incapable of penetrating the deep sites of wounds to activate clotting at the source of bleeding [9]. Therefore, developing a new hemostatic strategy for treating severe combat trauma remains a significant challenge.

Generally, more than 90% lethal hemorrhages caused by small-caliber firearms or improvised explosive devices occur in truncal and junctional vessels [2]. These severe wounds may form shapes that are similar to those of a vase (a small entrance with a large inner cavity

containing multiple bleeding sites) [10], which are harder to control than deep narrow or other irregular wounds. The formation of this vase-type wound is mainly caused by bullets or fragments with high velocities and impulse forces, which change from a linear to an inverted motion after entering the body due to tissue resistance. The inverted motion dissipates kinetic energy into the surrounding tissue, forming an inflated cavity inside the wound with massive hemorrhage [11]. Such vase-type wounds cause massive hemorrhaging and high mortality rates on the battleground because of their harsh environment involving high blood velocities, branched hemorrhages, multiple bleeding sites, and less accessible inner structures [12]. Moreover, most current hemostats can only block the vase-neck and cannot easily reach the deep sites of the inflated cavity, leading to a high pressure in the cavity, which destroys the unstable blood clot on the wound surface and results in failed hemostasis. Therefore, treating the harsh environment of vase-type wounds to enable the transportation of hemostats into deep sites is critical for controlling bleeding and reducing combat casualties.

Numerous advances have been made to prepare hemostatic materials that exert coagulation effects to prevent bleeding from the source. In a previous study, a shape-memory sponge was injected into the hemocoel and clot blood by swelling and physical pressing [13]. Furthermore, XStat™, a commercial hemostatic material, can rapidly swell and fill deep complex wounds. Nevertheless, it is extremely difficult to fill secluded and outstretched sites of irregular wounds, which may easily cause secondary bleeding due to overexpansion of the narrow position of wounds [14]. In other strategies, micro/nanoparticles transported the hemostats against the blood flow [15]. Although such particles possess good adaptability to complex wound environments owing to their micro-sizes and large specific surface areas, the harsh environment of complex wounds has extremely limited their application. Accordingly, designing a new strategy to address the conflict between the transportation of hemostats into deep sites and the complex wound environment is a key factor for achieving hemostasis in vase-type wounds.

To address these intractable issues, our group took inspiration from modern weapons. The torpedo, a weapon that can be navigated and guided to attack targets underwater, is capable of a high hit rate, large explosion power, and extended attack range [16]. The programmed process of navigation and deferred torpedo blast inspired us to create an ideal hemostatic delivery microplatform for the hemostasis of vase-type wounds through two procedures: (i) controllable actuation by strong and sustained impetus through the vase-neck of wounds against blood flow and (ii) "blast" generation after reaching the targeted deep sites for the burst release of hemostats and the acceleration of hemostatic diffusion to improve hemostatic efficiency. This delivery microplatform equipped with navigation and "blast" systems, inspired by the principle of a torpedo, is highly suitable for the delivery of hemostats into vase-type wounds through continuous penetration and rapid diffusion of hemostats inside the inflated cavity. To the best of our knowledge, there are no earlier scientific studies on the construction of a delivery microplatform based on the principle of torpedoes. Thus, to transform this active delivery microplatform from a proof-of-concept to actual products, significant technological challenges must be solved.

For decades, extraordinary progress has been made in the propulsion of drug delivery microplatforms using different driving forces, such as ultrasonic pulses [17], magnetic forces [18], gas propulsion [19] and motile bioorganisms [20]. Among these strategies, magnetic-mediated navigation, owing to its powerful, controllable, and sustained propulsion, has been widely studied for the precise delivery of cargo to the right position in blood fluids [21]. For example, magnetically driven microrollers were precisely actuated and steered via an external magnetic field and could swim against physiological blood velocities up to 2.5 dyn/cm^2, achieving targeted active drug transportation against the blood flow [22]. Thus, a continuous driving force produced by an external magnetic field as a navigation system can be used to move delivery microplatforms against blood flow [23]. However, because of branched hemorrhage, multiple bleeding sites, and less accessible inner

structure of vase-type wounds, it is difficult to precisely control the magnetic field to propel the delivery microplatform to reach multiple bleeding sites at different positions, which leads to an uneven distribution of hemostats and decreased contact area between blood and hemostats.

To accelerate the diffusion of hemostats inside the inflated cavity, which increases the contact between hemostats and deep bleeding sites, a deferred "blast" system should be introduced to generate secondary propulsion. Gas microgenerators based on local chemical reactions not only act as engines but also enable explosions, thus inducing the burst release of cargo and increasing the contact area between the cargo and bleeding site [24]. For example, CO_2 bubbles were used as microjet engines to propel $CaCO_3$ microplatforms against blood flow to accelerate the diffusion of thrombin (TH) inside the whole wound chamber [25]. Therefore, the construction of a hemostat delivery microplatform inspired by the principle of torpedoes may be established by combining magnetic navigation with gas propulsion to achieve continuous locomotion through the vase-neck of wounds and deferred drug diffusion in the deep sites of the inflated cavity. Nevertheless, integrating both features into a platform with programmed sequential action is a crucial challenge that needs to be solved urgently.

Here, inspired by the principle of deep underwater attack torpedoes, we prepared novel multifunctional microcluster (MC) colloidosomes equipped with navigation and "blast" systems. Upon the application of a magnetic field, MC colloidosomes can actively pass through the vase-neck of wounds and transport active drugs into inflated cavities to rush blood flow. Simultaneously, a "blast" is produced by releasing CO_2 bubbles to accelerate the diffusion of hemostats throughout the inflated cavity, thus activating clotting at the source of bleeding. To synthesize MC colloidosomes, positively charged composite particles (CF@PEM-RGD) comprising $CaCO_3/Fe_2O_3$ (CF) coated with RGD-modified polyelectrolyte multilayers (RGD-PEMs) and negatively charged zwitterionic carbon dots (CDs) were co-assembled at the oil/water interface at neutral pH to form MC colloidosomes (MC-CF@PEM-RGD) with a diameter of 36.59 ± 9.3 μm, which could instantaneously disassemble in the presence of acid due to the rapid charge reversal of zwitterionic CDs. Furthermore, MC-CF@PEM-RGD showed good adaptability to complex wounds owing to its micro-size, which endows the particles with a large specific surface area and increased contact area with platelets, red blood cells, and bleeding sites. Subsequently, MC colloidosomes were loaded with TH and then doped with a solid organic acid, protonyltranexamic acid ($TXA-NH_3^+$), to obtain composite microparticles (Fig. 1A). Once microparticles are applied to the bleeding site, a series of programmed processes are initiated: (i) composite microparticles are propelled by magnetic field navigation against the blood flow into the deep sites of vase-type wounds. (ii) H^+ release after the dissolution of $TXA-NH_3^+$ in blood decreases the local pH to trigger the charge reversal of zwitterionic CDs, resulting in the instant disintegration of colloidosomes and rapid release of TH. (iii) CO_2 bubbles released from the reaction between $CaCO_3$ and H^+ lead to a "blast" that accelerates the diffusion of TH and RGD-modified PEM capsules further to the bleeding sites, thus inducing a coagulation cascade inside the cavity (Fig. 1B and Supplementary movie 1). This study, based on the principle of torpedoes to achieve a programmed process for the hemostasis of vase-type wounds, offers a novel strategy for the treatment of massive bleeding on the battlefield.

Supplementary video related to this article can be found at https://doi.org/10.1016/j.bioactmat.2022.01.002

2. Materials and methods

2.1. Materials

Dextran-fluorescein isothiocyanate (FITC, 4 kDa), dextran-rhodamine B isothiocyanate (RBITC, 4 kDa), N-hydroxysuccinimide (NHS), and 1-(3-dimethylaminopropyl)-3-ethylcarbodiimide (EDC·HCl) were purchased from Sigma-Aldrich (Shanghai, China). The linear
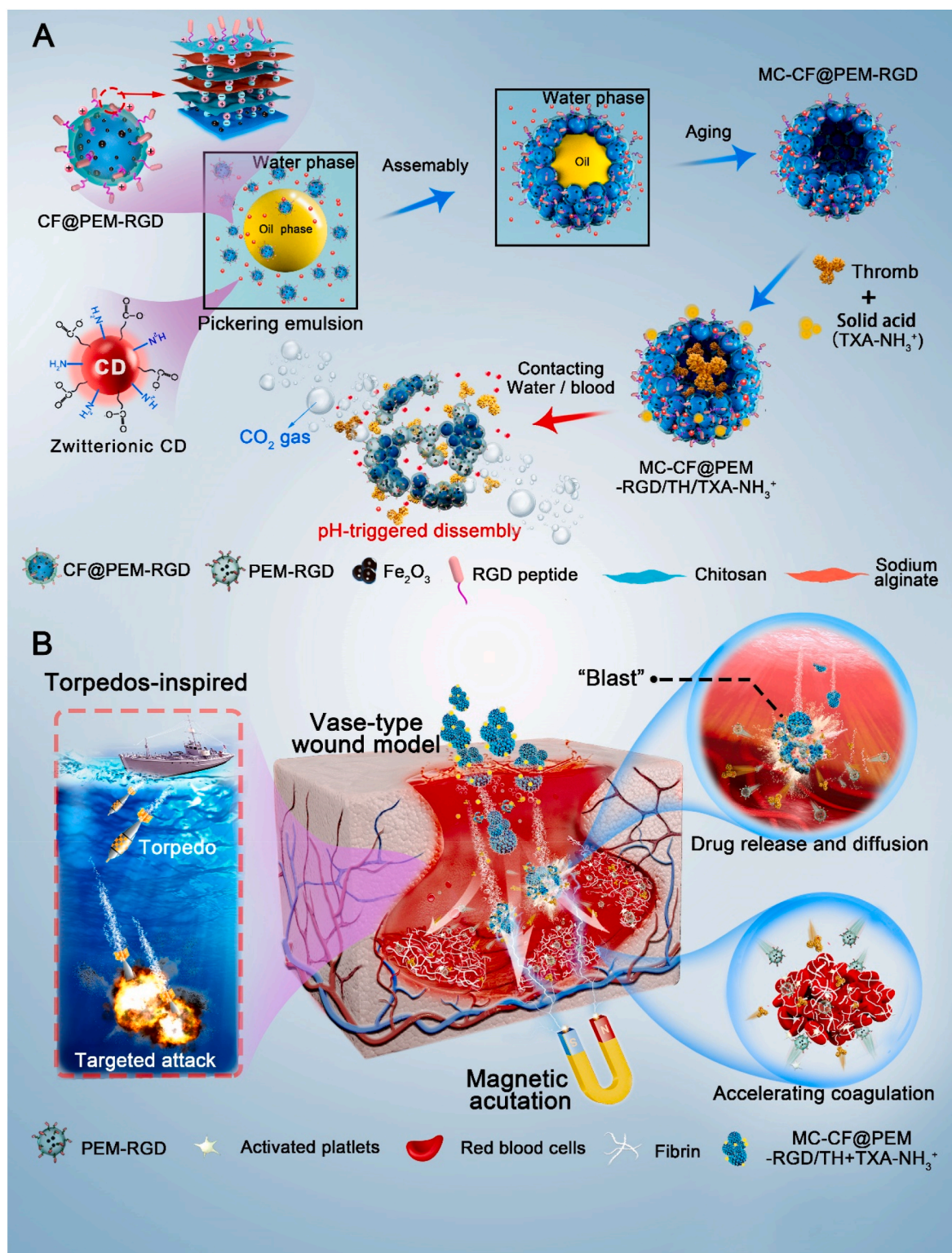
Fig. 1. MC colloidosomes for targeted hemostat delivery. Schematic of torpedo-inspired MC-CF@PEM-RGD based on magnetic navigation and gas propulsion for hemostat delivery into vase-type wounds. (**A**) Fabrication procedure of MC-CF@PEM-RGD/TH+TXA-NH$_3^+$ and its pH-triggered disassembly. (**B**) Programmed process of torpedoes, including navigation and targeted attacks via blasts. Inspired by this principle, MC-CF@PEM-RGD/TH+TXA-NH$_3^+$ was developed to locomote into deep sites against flowing blood by magnetic field navigation, then disassemble, and produce abundant CO$_2$ bubbles to accelerate the burst release and rapid diffusion of TH, thus achieving rapid coagulation in vase-type wounds.

fibrinogen-mimetic peptide GRGDS was synthesized by Bioss Antibodies Reagent Co., Ltd. (Beijing, China). CD41a-eFluor 450 and fibrinogen AF488 were obtained from Thermo Fisher Scientific (Shanghai, China). FITC-labeled chitosan (FITC-CS), citric acid (CA), and ethanediamine (EDA) were purchased from Ruixi Biotech Co. Ltd. (Xi'an, China). Magnetic iron oxide (Fe$_2$O$_3$, ~10 nm) was purchased from Macklin Reagent Co., Ltd. (Shanghai, China). Tranexamic acid (TA), chitosan (CS, MW: 20 K), sodium alginate (SA), and other reagents were obtained

from Aladdin Reagent Co., Ltd. (Shanghai, China) unless otherwise indicated.

2.2. Fabrication of CF@PEM-RGD

CaCO$_3$/Fe$_2$O$_3$ (CF) microparticles were synthesized by quickly adding 250 mL of a 0.33 M Na$_2$CO$_3$ solution to 250 mL of a 0.33 M CaCl$_2$ solution containing 10 mg/mL magnetic Fe$_2$O$_3$. The precipitated CF microparticles were washed with ethyl alcohol three times and dried at 70 °C for 2 h. The obtained CF powder was then stored at 25 °C. To prepare fluorescent CF microparticles loaded with dextran−RBITC (4 kDa), the fluorescent reagent (5 mg) was mixed with a CaCl$_2$ solution before preparing the CF microparticles. CS-RGD was synthesized using the EDC/NHS chemistry. GRGDS was dissolved in 2 mL of HAc-NaAc buffer solution (pH 6.0) at 10 mg/mL. NHS (50 mg) and EDC HCl (100 mg) were dissolved in the GRGDS solution and stirred at 4 °C for 6 h to activate the carboxyl groups. Then, 10 mg/mL of FITC-labeled CS-RGD in 1% HAc solution (pH 6) was added to the activated polymer solution and stirred overnight at 4 °C. The reaction solution was dialyzed (MWCO 3500 Da) for 3 d and then dried by freezing. CF@PEM-RGD microparticles were prepared using a layer-by-layer assembly method. Briefly, CF powder (5 g) was alternately treated with polymer layers of CS solution (500 ml, 0.5, pH 5.1) and SA (500 ml, 1 mg/mL, pH 5.1), resulting in the structure of (CS/SA)$_4$. Subsequently, CS-RGD (0.5 mg/mL) was deposited onto the surface of the aforementioned microparticles to form the final outer layer structure of (CS/SA)$_4$CS-RGD. After lyophilization, the resulting powder was stored at room temperature. Large-scale preparation of CF and CF@PEM-RGD powders can be achieved by directly increasing the above-mentioned preparation ratio.

2.3. Fabrication of zwitterionic CDs

The zwitterionic CDs were synthesized according to a previous study [26] by adding EDA and CA at different molar ratios (1:0.3, 1:0.5, 1:0.8, and 1:1) into a Teflon-lined autoclave containing 30 mL of aqueous solution. The mixture was then heated at 200° °C for 6 h. The resultant samples were dialyzed, lyophilized, and stored at 4 °C until further use. A large amount of CD powder could be obtained by directly increasing the above-mentioned preparation ratio.

2.4. Synthesis of dynamic microcluster colloidosomes and cargo loading

In a typical experiment, 0.9 g of CF@PEM-RGD was rapidly injected into 16 mL of zwitterionic CDs (2 mg/mL) under ultrasonication (20 kHz, 50 W) for 30 s. Then, 1.5 mL soybean oil was carefully added to the aforementioned solution, and the resultant mixture was stirred at a rotation speed of 10,000 rpm for 3 min using a modular homogenizer. The resultant water/oil Pickering emulsion was incubated at 28 °C for 12 h. Subsequently, the supernatant oil was gently removed, and 2 mL of tetrahydrofuran was added to replace the oil from the colloidosomes by standing for 15 min. After centrifugation, the colloidosomes were washed twice with tetrahydrofuran and washed three times with PBS. Subsequently, the colloidosomes were re-suspended in n-butyl alcohol and freeze-dried to obtain MC-CF@PEM-RGD powder.

For cargo loading, MC-CF@PEM-RGD and other control groups were resuspended at 10 mg/mL in phosphate-buffered saline containing TH (0.2 U/ml) or dextran RBITC (1 mg/mL). Dextran-RBITC (4 kDa) was used because its molecular weight is similar to that of TH (37 kDa). After incubation at 37 °C for 2 h, the resultant mixtures (MC-CF@PEM-RGD/TH) were washed and centrifuged to remove dissociative cargos and lyophilized for further use. The TH activity of the colloidosomes was measured according to a previous study using a chromogenic substrate assay (S-2238) [27]. The loading content (LC) was calculated using Eq. (1).

$$LC \ (U/mg) = \frac{Activity \ of \ thrombin \ in \ microparticles}{Weight \ of \ microparticles} \tag{1}$$

To prepare composite microparticles capable of disassembly and producing gas propulsion upon contact with blood, MC-CF@PEM-RGD/TH was physically mixed with TXA-NH$_3^+$ at a molar ratio of 1:1 (CaCO$_3$: TXA-NH$_3^+$). To prepare TXA-NH$_3^+$, TA solution (0.5 M, 500 ml) was prepared and its pH was adjusted to 4.0 by adding concentrated hydrochloric acid (HCl). Then, the TXA-NH$_3^+$ powder was collected by lyophilization. Notably, large amounts of this powder could be obtained by directly increasing the above-mentioned preparation ratio.

2.5. Characterization

Optical and fluorescence microscopy images were collected using an optical microscope (Eclipse Ni-E, Japan) and a laser scanning confocal microscope (LSCM, FV3000RS, OLYMPUS, Japan), respectively. Scanning electron microscopy (SEM) images and elemental mapping images were obtained using a Zeiss Gemini 300 (German) equipped with an EDS detector attached to the SEM instrument. Microparticles were coated with 80% Au and 20% Pd before observation at 15.0 kV. FTIR spectra of the CS-peptide conjugates were collected using a Bruker Alpha spectrometer (Bruker TensorII, Germany). XRD spectra were recorded using an XPert PRO MPD instrument (PANalytical, Dutch). The surface charge of the microparticles (zeta potentials) and size distribution were determined using a dynamic light scattering instrument (DLS, Nano S90, UK).

2.6. Cargo release

In the release assay, colloidosomes/TH and MC-colloidosomes/ dextran RBITC were rapidly added to the PBS solution (pH 7 or 4.5). At a specified time, 1 mL of the supernatant solution from each group was collected after centrifugation, and 1 mL of fresh PBS (pH 7.0 or 4.5) was replenished. The activity of TH released from the microparticles and the fluorescence intensity were detected via a chromogenic substrate assay (S-2238) and a fluorospectrophotometer (FLS9800 PANalytical, Netherlands), respectively.

2.7. Coagulation assay

The procoagulant activity of the different samples was assessed by observing the gel time of rabbit whole blood, according to a previous study [28]. In brief, 0.1 g of the samples and fresh anticoagulant blood (2 mL) were added to a centrifuge tube. Then, 80 μL of CaCl$_2$ (0.2 M) was rapidly added, and the coagulation time was recorded when the fluidity of blood was lost.

2.8. Actively controlled locomotion of MC-CF@PEM-RGD under static and dynamic conditions

The locomotion experiments were carried out in a closed micro-groove composed of poly (methylmethacrylate) (PMMA) with a micro-channel (200 μm height, × 10 mm width, × 30 mm length), which was designed using a cutting system (Xiandao, China). The fluidic connections in the PMMA bottom piece were achieved using a polyolefin thermoplastic elastomer (TPE) tube with an inner diameter of 0.3 mm. Before testing, the channel was washed with an aqueous HCl solution (2 M) and rinsed with PBS. MC-CF@PEM-RGD, mixed with PBS or fresh anticoagulant rabbit blood, was loaded into a syringe and introduced into the micro-groove using a syringe pump (LSP01-1A, Longer, China). Owing to the limits of the microscope, light cannot penetrate undiluted blood, leading to blurred images. Therefore, 4 × diluted blood samples were prepared by directly adding normal saline to the original blood. The flow speed was controlled within a range of 40–1080 μm/s.

2.9. Locomotion of MC-CF@PEM-RGD/TH doped with TXA-NH$_3^+$ in the presence of a magnetic field

To capture the motion of MC-CF@PEM-RGD, videos were captured at 10,000 frames per second (fps) using a high-speed camera with a 5 × objective lens. For the tests, a glass tube with a closed bottom (length of 5.5 cm and inner diameter of 4 mm) was filled with Tween-20 solution and fixed vertically, and a permanent magnet (1.0 T) was placed at the bottom of the glass tube. MC-CF@PEM-RGD/TH doped with TXA-NH$_3^+$ in powder form was fed into the channel, and the locomotion of the microparticles was observed. To observe the diffusion of the microparticles in the horizontal direction, a beaker (height of 5.5 cm and inner diameter of 4 cm) filled with Tween-20 solution was employed, and the locomotion was imaged using the same method.

The locomotion of the MC-CF@PEM-RGD/TH doped with TXA-NH$_3^+$ in powder form was also assessed using an *in vitro* microfluidic device combined with a microscope system under magnetic guidance. A side outlet tee (inner diameter of 4 mm) was connected at the end of the injection pump via a TPE tube, and a permanent magnet ((1.0 T)) was set on the side of the tee close to the entrance of the blood flow (Fig. 5F). Fresh blood containing an anticoagulant was injected into the channel of the tee positioned at 0°, 45°, 90°, 135°, and 180° at controlled flow speeds (0.5–30 mm/s) using a syringe pump. For the tests, 0.2 g of MC-CF@PEM-RGD combined with TXA-NH$_3^+$ in powder form was fed from the side outlet of the tee. After 15 s, the accumulated samples in the tested region were detected using a microscope.

2.10. Platelet and erythrocyte adhesion

Quantitative analysis of the adhesion efficiency of platelets and erythrocytes was conducted as described in our previous study [8]. Briefly, fresh erythrocytes and platelet-rich plasma were separated from rabbit blood via centrifugation (1500 rpm, 5 min). For erythrocyte adhesion, 100 μL of fresh erythrocyte suspension was mixed with 0.1 g of microparticles for 1 h at 37 °C. As a control, 100 μL of erythrocyte suspension was directly added to water. Next, the microparticles were washed with PBS solution thrice and then transferred into pure water. After 1 h of incubation, the supernatant was obtained, and its OD$_{540}$ was evaluated using a microplate reader (Epoch2, USA). The percentage of erythrocytes was calculated using the following equation:

$$\text{Erythrocyte adhesion } (\%) = \frac{OD_{540} samples}{OD_{540} control} \qquad (2a)$$

For platelet adhesion, platelet-rich plasma was dropped on the surface of 0.1 g microparticles. After 1 h of incubation, the mixture was washed thrice with PBS solution and then treated with Triton X-100 solution (1%) to lyse platelets. The lactate dehydrogenase (LDH) enzyme in the resulting suspension was evaluated using an LDH kit (Biyuntian, China). The number of adherent platelets was calculated according to LDH enzyme concentration.

Additionally, SEM was used to observe platelet and erythrocyte adhesion. To further study the role of RGD, the aggregation of activated platelets on the surface of the RGD-PEM capsules was evaluated by mixing 1 mL of FITC-labeled capsule solution (~1 million), platelets (0.5 mL) obtained from a mouse (50 million, stained with CD41a-eFluor 450), fibrinogen (0.5 U/mL), and 5 mM CaCl$_2$. After incubation at 37 °C for 10 min, the mixture was analyzed using flow cytometry (Thermo Fisher Scientific, USA).

2.11. Dynamic binding assays

The activated platelets attached to the surface of the capsules under dynamic conditions were evaluated in a microfluidic chamber, which was fabricated according to a previous study with a few modifications [29]. The glass slide at the bottom of the chamber was washed with 2 M HCl aqueous solution, rinsed with PBS, and immersed in collagen (0.5

mg/mL) and ADP (50 μg/mL). The glass slide was then deposited in an incubator at 37 °C for 2 h. Additionally, the chamber was vacuum-sealed and connected to a programmable pump via a TPE tube to maintain fluid flow. For the dynamic binding assays, equal volumes of mouse platelets (50 million/mL) stained with CD41a-eFluor 450 and fluorescein isothiocyanate (FITC) were injected into the chamber at 10 mm/s for 10 min.

2.12. Hemostatic performance using in vitro bleeding model

The *in vitro* bleeding model was fabricated using traditional reverse mold and photolithographic techniques. For device assembly, polydimethylsiloxane (PDMS, Sylgard 184) was poured into square grooves (6.5 cm × 4.5 cm × 5.5 cm), and a curing agent was added at a weight ratio of 10:1. After baking at 80 °C for 3 h, a model with a specially shaped channel (Figs. 7A and S10) was obtained. The joints were treated with a biopsy punch to form holes with a sectional area of ~0.25 cm^2, ensuring that blood could access the channel at the same flow speed. Before the tests, a permanent magnet (1.0 T) was positioned at the bottom of the model. Fresh anticoagulant blood was injected at different flow speeds (0.5–30 mm/s), and 1 g of powder for all groups was initially fed at the top of the model. The time taken to block the bleeding points and recover the blood flow was recorded as the coagulation time. If the blood seeped from the top of the powder, another 0.5 g of powder was added until the bleeding points were blocked. Furthermore, the distribution of microparticles around the bleeding point was evaluated using microscopy and SEM. Each experiment was repeated five times.

2.13. Hemostatic performance in a rabbit model of liver hemorrhage

All experiments, including animal studies, were performed in compliance with the protocols approved by the National Center of Animal Science Experimental Teaching of Southwest University of China (accreditation number of the laboratory/investigator: CQLA-2019-0281). A vase-type wound with a small entrance and large inner cavity was made on the liver using a No. 12 knife with a crooked tool nose. The liver bleeding model was subjected to different treatments: (I) gauze, (II) Celox™, (III) MC-CF@PEM-RGD/TH + TXA-NH$_3^+$, (IV) MC-CF@PEM-RGD/TH with magnetic field, (V) MC-CF@PEM-RGD/TH + TXA-NH$_3^+$ with a magnetic field, and (VI) MC-CF@PEM/TH + TXA-NH$_3^+$. The microparticles in powder form (2 g) were directly applied to the wound without pressure. The time taken to stop blood flow from the wound was recorded as the coagulation time. To characterize the magnetic actuation and propulsion of the particles, FITC-labeled particles of different groups were applied to the bleeding model. After bleeding ceased, the livers were immediately harvested, fixed with formalin (10%), and sectioned vertically for hematoxylin-eosin (HE) staining and immunofluorescence histochemical staining. Each experiment was repeated five times.

2.14. Evaluation of cytotoxicity and hemolysis and in vivo degradation

The cytotoxicity of MC-CF@PEM-RGD was determined using mouse fibroblast cells (L929). Various microparticles were exposed to UV radiation for sterilization and added to a 96-well plate containing 200 μL cell suspension (10^4 cells/well). The concentrations were adjusted to 5, 10, 30, 50, and 100 μg/mL. After incubation for 24, 48, and 72 h, cytotoxicity was evaluated using the Cell Counting Kit-8 (CCK-8). L929 cells without treatment served as the blank control group. The effect of microparticles on L929 cells was evaluated using a live/dead (Calcein-AM/PI) cell double staining kit. Each experiment was repeated five times [30].

For hemocompatibility evaluation, RBCs were obtained from fresh rabbit anticoagulant blood via centrifugation and diluted to 4% (v/v) with PBS. Twenty milligrams of microparticles and 1.5 ml of diluted RBCs were added into the centrifuge tube. After incubation for 2 h at

37 °C, the supernatant was collected by centrifugation. The UV absorbance at 545 nm was measured using a UV–vis–NIR absorbance spectrometer (400–900 nm). PBS and distilled water served as the positive and negative controls, respectively. The hemolysis ratio was calculated according to a previously reported method [31]. Each experiment was repeated thrice.

The degradation performance of MC-CF@PEM-RGD was evaluated using a rabbit liver implantation model and a muscle implantation model. Before implantation, the rabbit was anesthetized, and the fur on the back and manitrunk was shaved. For liver implantation, a 5 mm incision was created on the liver, and 20 mg of the sample was added, followed by a suture to maintain the sample inside the liver. Similarly, a 10 mm incision was created on the back of the rabbit, and 50 mg of the sample was encapsulated inside the muscle via sutures. At the desired interval (2, 4, 6, and 8 weeks), the rabbit was sacrificed, and the tissue around implantation was excised for histological analysis. Additionally,
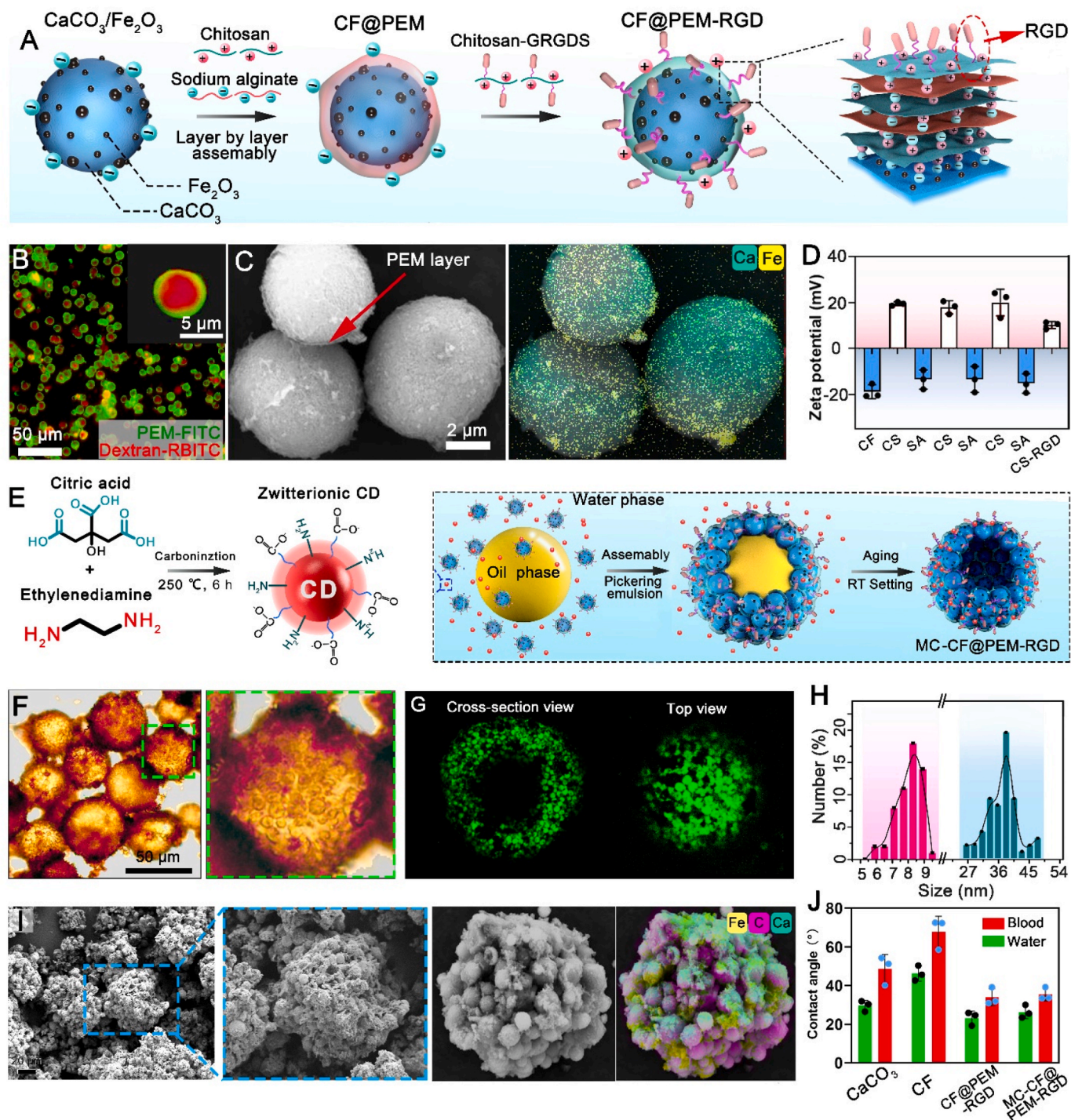

Fig. 2. Design and characterization of the MC colloidosomes. (**A**) Schematic diagram illustrating the fabrication of CF@PEM-RGD. (**B**) LSCM images of CF@PEM-RGD. (**C**) SEM and mapping images of CF@PEM-RGD. (**D**) Zeta potential during the layer-by-layer assembly procedure. (**E**) Schematic diagram illustrating MC-CF@PEM-RGD based on Pickering emulsion. Microscopy images (**F**) and CLSM 2D images (**G**) of the cross section and top surface of MC-CF@PEM-RGD. (**H**) Size distribution of CF@PEM-RGD and MC-CF@PEM-RGD. (**I**) SEM and mapping images of MC-CF@PEM-RGD. (**J**) Contact angle for water drops (5 μL) on the surface of the particles in powder form.

commercial hemostatic materials (CeloxTM, USA) served as the control group [32].

3. Results and discussion

3.1. Design and characterization of MC colloidosomes

MC colloidosomes were assembled using a facile emulsion templating approach. Here, we utilized the electrostatic interactions between positively charged CF coated with functional RGD-PEM and negatively charged zwitterionic CDs to synthesize stable MC colloidosomes (MC-CF@PEM-RGD), which rapidly disassembled under acidic conditions because of the charge reversal of zwitterionic CDs. The magnetically responsive CF particle core was used as a template for polyelectrolyte deposition via co-precipitation reactions. SEM and elemental mapping images indicated that Fe_2O_3 NPs were distributed on the surface of calcium carbonate (Fig. S1A). The X-ray diffraction (XRD) pattern of CF showed distinct diffraction peaks of vaterite (020, 120, and 220) and ferric oxide (104, 110, 006, 202, and 204), indicating that the crystalline phase of $CaCO_3$ was not affected by the introduction of ferric oxide (Fig. S1C). The outer polyelectrolyte layers were deposited onto the CF microparticles via a layer-by-layer (LBL) assembly (Fig. 2A). The laser scanning confocal microscopy (LSCM) images (Fig. 2B) showed a distinct core-shell structure composed of an inner core with a thin outer layer, indicating that the CF core (loaded with dextran-FITC) was encapsulated by RGD-PEM (labeled with dextran-RBITC). After the deposition of RGD-PEM, a thin layer covered the surface of the CF particles and a smooth surface of PEM was observed (Fig. 2C); the physical dimensions of the inner core of CF increased from 4.19 ± 0.73 μm to 5.08 ± 2.31 μm. Furthermore, EDS and mapping images showed that the Fe content of CF@PEM-RGD significantly decreased, which might be due to the repeated vibration and cleaning of the LBL assembly process (Fig. S1B). The successful deposition of alternate polyelectrolyte layers with opposite charges on the surface of the CF particles was supported by zeta potential measurements (Figs. 2D and S1E). The final charge on CF@PEM-RGD was positive, indicating the presence of chitosan-RGD. Meanwhile, in the FTIR spectrum, the absorption peaks at 1600.3 cm^{-1} and 1651.5 cm^{-1} were ascribed to the N-monosubstituted amide vibrations, revealing the existence of ester groups. This demonstrated that the RGD peptide was conjugated to the amino groups of chitosan via ester groups through the EDC/NHS chemistry (Figs. S1D and S1F). The introduction of RGD enabled CF@PEM-RGD to target the activated platelets, even with the high shear of blood flow, owing to the strong specific interaction between RGD and platelet membrane glycoprotein Contact angle [33].

Zwitterionic CDs with excellent biosafety were obtained through a hydrothermal reaction by condensing ethanediamine (EDA) and citric acid (CA) at 200 °C, according to the method described in a previous study [34]. The amino group of EDA and the carboxyl group of CA on the surface of the CDs endowed them with pH sensitivity: the negative charge on the surface switches to a positive charge at pH changes below the isoelectric point [35]. By adjusting the molar ratio of EDA and CA, the isoelectric point can be flexibly controlled, and in this study, a molar ratio of 1:0.5 was chosen to prepare zwitterionic CDs with an isoelectric point of pH 4.5 (Fig. S2A). Subsequently, these two particles with opposite charges were used to fabricate dynamic colloidosomes in an oil/water emulsion (Fig. 2E). The surface zeta potential of MC-CF@PEM-RGD was neutralized, which may have been induced by charge neutralization (Fig. S2C). The microscopy images indicated that spherical MC-CF@PEM-RGD with a diameter of 36.59 ± 9.3 μm was successfully fabricated (Fig. 2F and H). After lyophilization, the CLSM 2D images of the cross-section and top view indicated that the interior of MC-CF@PEM-RGD was hollow (Fig. 2G). Furthermore, the SEM images indicated that MC-CF@PEM-RGD was stable even after vacuum drying, suggesting that strong interactions existed between the particles (Fig. 2I). As shown in Fig. 2J, the water and blood contact angles of

MC-CF@PEM-RGD were $26.3 \pm 2.75°$ and $35.4 \pm 2.70°$, respectively. In contrast, the hydrophilicity increased after deposition of RGD-PEM, which may have been caused by the hydrophilicity of chitosan and sodium alginate. Based on earlier studies, we hypothesized that the assembly of the colloidosomes in our study was determined by two main factors [36]: (i) the high interfacial adsorption energy due to the partial hydrophobicity of CF@PEM-RGD and (ii) the electrostatic interaction between CDs and CF@PEM-RGD. To validate the assembly mechanism, only CF@PEM-RGD particles were used, and the resultant colloidosomes maintained their structure in the emulsion, although the drying process led to structural collapse (Fig. S2B). Therefore, colloidosomes cannot be formed with only one type of charged particle, which confirms that both CDs and CF@PEM-RGD are essential for the fabrication of MC-CF@PEM-RGD.

3.2. pH-triggered destabilization and disassembly

The pH-triggered destabilization of MC-CF@PEM-RGD was initially investigated using a microscope. To record the process of pH-triggered disassembly and drug release, a solid acid TXA-NH$_3^+$ aqueous solution (0.5 M, pH 4.5) was added to the MC-CF@PEM-RGD/TH drop on a glass slide. As expected, MC-CF@PEM-RGD was well dispersed in an aqueous solution (pH 7.0). However, once the TXA-NH$_3^+$ aqueous solution was added, the colloidosomes immediately destabilized and thoroughly disassembled within 30 s (Fig. 3B and Supplementary Movie 2). Meanwhile, $CaCO_3$ self-dissolved in the presence of TXA-NH$_3^+$, releasing CO_2 and leaving RGD-modified PEM (RGD-PEM) capsules. To further illustrate the disassembly process, MC-CF@PEM-RGD loaded with a fluorescent cargo (dextran-RBITC) was treated with TXA-NH$_3^+$, and the red fluorescence diminished and rapidly spread to the surrounding, demonstrating the burst release of fluorescent cargo (Fig. 3C). Moreover, MC-CF@PEM-RGD doped with TXA-NH$_3^+$ (in powder form) was directly placed into water, and MC-CF@PEM-RGD disintegrated from the center into individual capsules, which were then propelled by CO_2 gas (Supplementary Movie 3). This disintegration process resembled a "blast," which favored the release and diffusion of hemostats after the colloidosomes were actuated into the deep sites of wounds.

Supplementary video related to this article can be found at https://doi.org/10.1016/j.bioactmat.2022.01.002

The solution containing the disassembled particles was examined by high-resolution microscopy and SEM, and the images showed that the RGD-PEM capsules disintegrated into shell pieces. This is mainly caused by the CO_2 gas strike (Fig. 3D). The disassembly mechanism was investigated by measuring the charge variation of the CDs and CF@PEM-RGD at pH values of 4.0–7.5 (Fig. 3E). The results showed that CF@PEM-RGD was always electropositive, while the charge of the CDs was reversed at pH 4.5, indicating that the electrostatic repulsion between the CDs and CF@PEM-RGD under acidic conditions caused disintegration of the colloidosomes. In addition, the diminished mechanical properties due to the decomposition of $CaCO_3$ and the propulsion effect of CO_2 bubbles might synergistically promote the disintegration of the colloidosomes.

To further characterize the drug loading capacity and pH-triggered drug release profile, TH and fluorescein dextran-RBITC as model drugs were used to visualize the loading and release processes. MC-CF@PEM-RGD/TH was prepared using a feeding ratio of 1 mg:0.02 U. The drug encapsulation efficiency and loading content of CO-CF@PEM-RGD were much higher than those of single CF@PEM-RGD, reaching approximately 70% and 0.01 U/mg, respectively (Fig. 3F). To gain a better visualization of the release mechanism, the fluorescein model drug was loaded. As shown in Fig. 3G, fluorescein dextran-RBITC release from MC-CF@PEM-RGD exhibited good pH dependence. Approximately 30% of dextran-RBITC was released over a period of 30 min at pH 7.0, while more than 60% of the drug was released within 1 min at pH 4.5, indicating excellent drug release at low pH. Similarly, the release profile of TH showed that more than 60% of the TH was released within 120 s
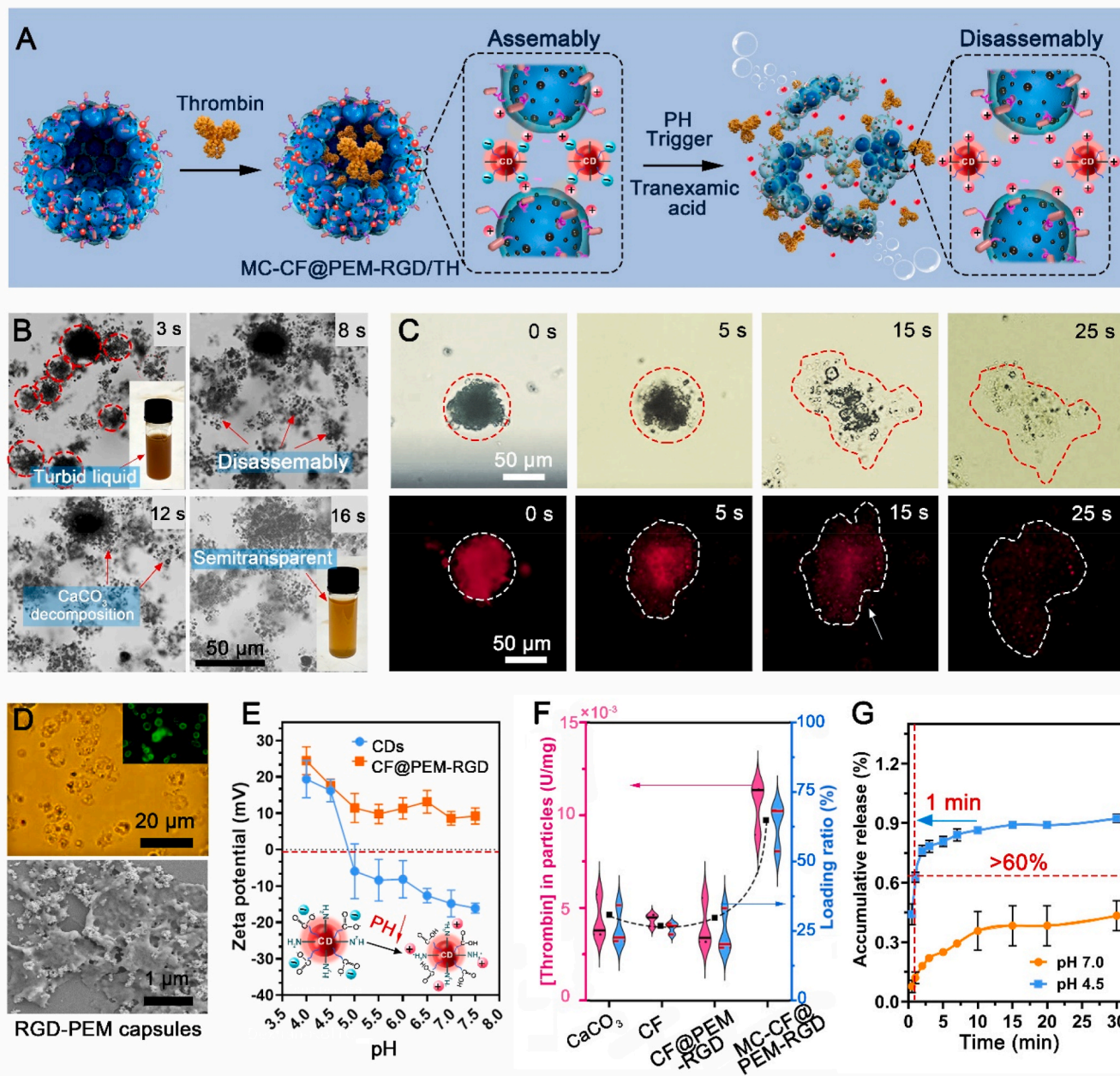
Fig. 3. Thrombin loading and pH-triggered disassembly of the MC colloidosomes. (**A**) Schematic illustrating thrombin loading and the pH-triggered disassembly of MC-CF@PEM-RGD due to the reversal of electrostatic attraction between CF@PEM-RGD and the CDs by TXA-NH_3^+ stimulation. (**B**) pH-triggered disassembly process of MC-CF@PEM-RGD. (**C**) pH-triggered burst release of MC-CF@PEM-RGD. Fluorescence signals from dextran-RBITC. (**D**) Microscopy and SEM images of RGD-modified PEM capsules after disassembly. (**E**) Zeta-potential of CF@PEM-RGD and CDs in the pH range of 4–7.5. (**F**) Thrombin encapsulation efficiency and loading content of CO-CF@PEM-RGD. (**G**) Release profile of dextran-RBITC at pH 4.5 and 7.0.

(Fig. S3D). Furthermore, the results of the coagulation assay showed that MC-CF@PEM-RGD/TH doped with TXA-NH_3^+ displayed superior procoagulant activity, with a coagulation time of 92.0 ± 9.4 s, which was approximately two times faster than that of MC-CF@PEM-RGD/TH + TA (Fig. S3A). This result demonstrated that TXA-NH_3^+ facilitated the burst release of TH from MC-CF@PEM-RGD/TH upon contact with blood and did not influence TH activity. In addition, CF@PEM-RGD showed an enhanced hemostasis effect in comparison with CF@PEM, which indicated that the introduction of RGD peptide could accelerate the coagulation process. The disassembly and burst release performance of the MC colloidosomes stimulated by acid ions are summarized in Fig. 3A. The electrostatic repulsion and CO_2 propulsion effect stimulated by TXA-NH_3^+ resulted in a "blast" that disintegrated the colloidosomes,

leading to the burst release and rapid diffusion of the encapsulated hemostats. SEM observation showed that even after storage for six months at −20 °C, MC-CF@PEM-RGD/TH/TXA-NH_3^+ in powder form still maintained a stable structure, indicating no significant influence on the morphology of MC-CF@PEM-RGD after the introduction of TH and TXA-NH_3^+ (Fig. S3B). Furthermore, there was no significant change in the coagulation activity of MC-CF@PEM-RGD/TH/TXA-NH_3^+ before and after storage (Fig. S3C).

3.3. Magnetically controlled locomotion and mathematical model describing the locomotion of MC-CF@PEM-RGD

To overcome the high blood flow originating from inside the vase-

type wounds, magnetic-mediated navigation was employed to carry the MC-CF@PEM-RGD against blood flow to penetrate deep wound sites. To confirm the magnetic responsive performance of MC-CF@PEM-RGD, a microfluidic device was used (Figs. 4A and S3E). In addition, a permanent magnet with a magnetic field intensity of 1 T was employed to evaluate the magnetic responsive performance and hemostasis properties of MC colloidosomes. As shown in Fig. 4B and C, MC-CF@PEM-RGD in static blood (4 × diluted) moved along the magnetic field at a speed of 287.8 ± 48.4 μm/s and altered its direction when the orientation of the magnetic field (1.0 T) changed (Supplementary Movie 4). CF@PEM-RGD also achieved locomotion in blood at a low speed of 25.8 ± 7.2 μm/s (Fig. 4C and Supplementary Movie 5). Because of the complex environment of the bleeding site, MC colloidosomes need to overcome the resistance of blood flow to reach deep bleeding sites. To further demonstrate that the navigation of the colloidosomes was actively controlled in a more practical way, their upstream speeds were measured in blood (4 × diluted) flowing at speeds of 40–1080 μm/s. We first measured the upstream speed of different microparticles in the blood and PBS flowing at various speeds (Fig. 4D and E). As expected, for both microparticles, the upstream traveling speed in blood was lower than that in PBS because of the high viscosity of blood, and as the flow speed increased, the upstream speed decreased. In addition, when the blood flow speed increased to 72 μm/s, the upstream speed of CF@PEM-

RGD decreased to 0 μm/s (Fig. 4F and Supplementary Movie 6). In contrast, MC-CF@PEM-RGD was able to move against the flow even at a flow speed of 720 μm/s. In addition, as shown in Fig. 4G and Supplementary Movie 7, MC-CF@PEM-RGD floated along the direction of blood flow before a magnetic field was applied; however, with the application of a magnetic field, MC-CF@PEM-RGD was able to swim through flowing red blood cells, which supported the above-mentioned results. These results demonstrate that the locomotion capacity of MC-CF@PEM-RGD was superior to that of CF@PEM-RGD under the same magnetic field strength.

Supplementary video related to this article can be found at https://doi.org/10.1016/j.bioactmat.2022.01.002

To understand the locomotion behavior of MC-CF@PEM-RGD, a mathematical model was established, as shown in Fig. 4H. The motion of an individual MC-CF@PEM-RGD on the x–y surface is mainly manipulated by the magnetic force ($\mathbf{F_m}$) and drag force ($\mathbf{F_d}$) of the surrounding fluid. $\mathbf{F_m}$ is usually calculated using Equations (2) and (3) [37,38], while $\mathbf{F_d}$ is calculated using Equation (4) [39]:

$$\mathbf{F_m} = \nabla(\mathbf{m} \cdot \mathbf{B}) \tag{2b}$$

$$\mathbf{m} = \frac{3V_m}{\mu_0}\left(\frac{\mu - \mu_0}{\mu + 2\mu_0}\right)\mathbf{B} \tag{3}$$
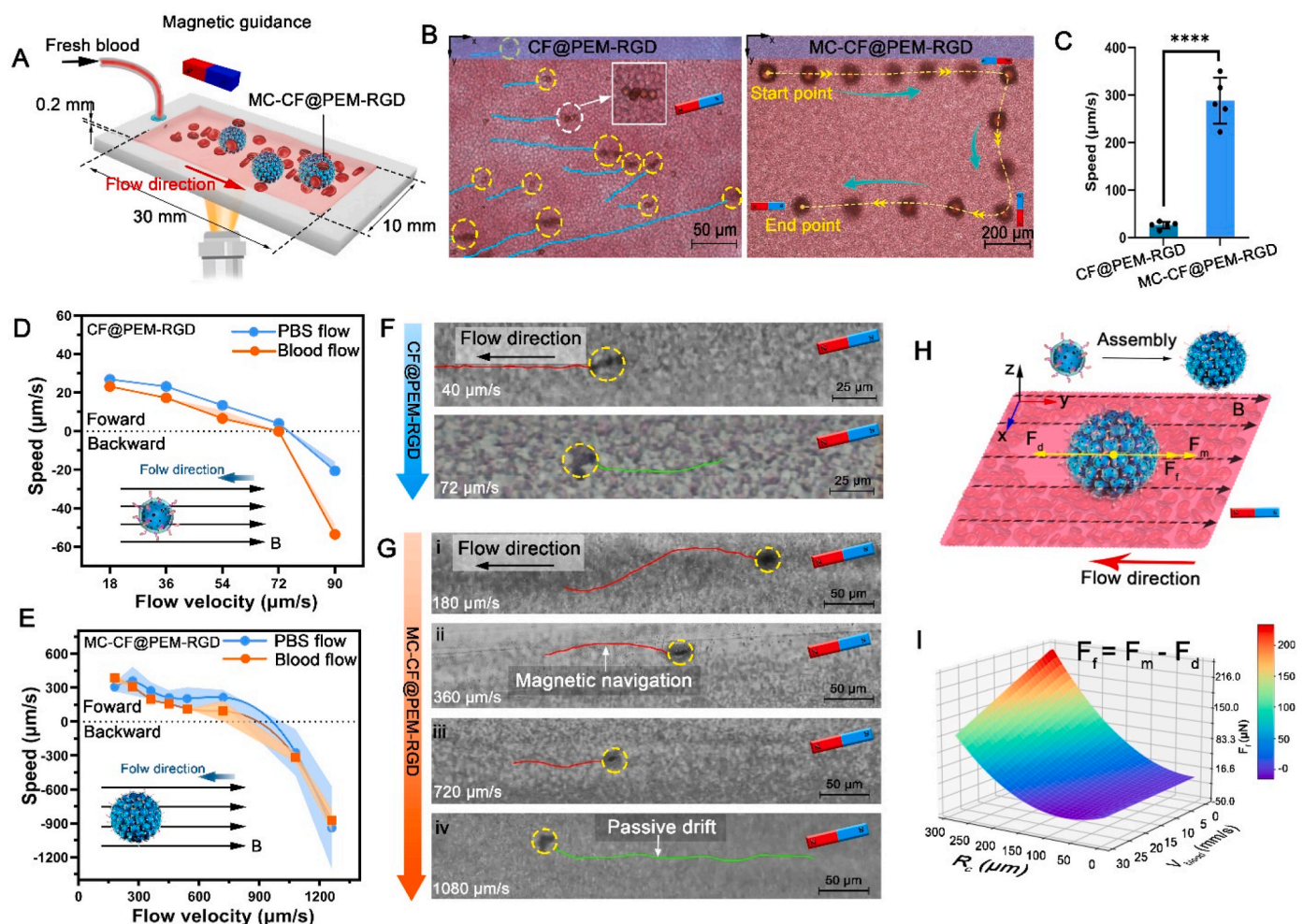

Fig. 4. Magnet-mediated locomotion of the MC colloidosomes. (**A**) Schematic diagram of the micro-fluidic device. (**B**) Magnet-mediated navigation of CF@PEM-RGD and MC-CF@PEM-RGD. (**C**) Average speeds of the microparticles, n = 5, ****P < 0.0001. Upstream speeds of CF@PEM-RGD (**D**) and MC-CF@PEM-RGD (**E**) in PBS and blood (4 × diluted) flowing at different speeds under an applied uniform magnetic field. Tracks of CF@PEM-RGD (**F**) and MC-CF@PEM-RGD (**G**) in blood (4 × diluted) flowing at different speeds. (**H**) Schematic of the locomotion mechanism of MC-CF@PEM-RGD. (**I**) Total acting force ($\mathbf{F_f}$) experienced by the inclusion diameter of Fe content within MC-CF@PEM-RGD.
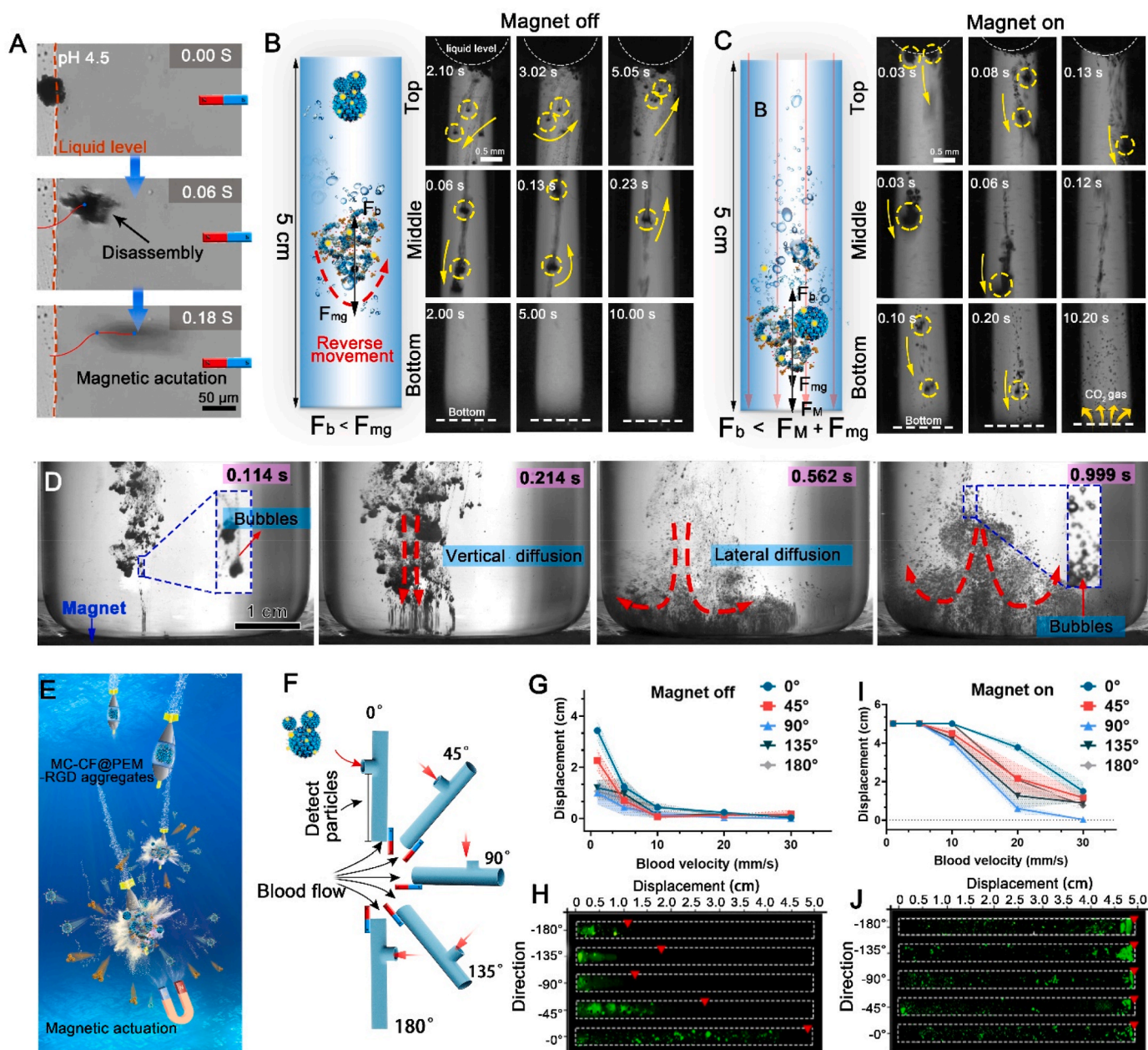
Fig. 5. Locomotion of the colloidosomes with magnetic actuation and TXA-NH$_3^+$-initiated propulsion. (**A**) Displacement of an individual MC-CF@PEM-RGD/TH upon magnetic field application after contacting the TXA-NH$_3^+$ solution (pH 4.5). Images of MC-CF@PEM-RGD doped with TXA-NH$_3^+$ moving downward in the absence (**B**) and presence (**C**) of a magnetic field. F$_b$: buoyancy; F$_{mg}$: gravity; F$_M$: magnetic force. (**D**) Time-lapse frames (0–1 s) of the lateral and vertical locomotion of MC-CF@PEM-RGD with the application of a magnetic field. (**E**) Hemostat delivery strategy inspired by the attack action of torpedoes. (**F**) Schematic illustrating the displacement of MC-CF@PEM-RGD in blood flowing at different velocities. (**G, H**) Upstream displacement of FITC-labeled MC-CF@PEM-RGD/TH with and without the application of a magnetic field. (**I, J**) Distribution of FITC-labeled MC-CF@PEM-RGD/TH in blood flowing at 10 mm/s with and without the application of a magnetic field.

$$\mathbf{F_d} = -6\pi\eta R_c(\boldsymbol{v_c} - \boldsymbol{v_{blood}}) \tag{4}$$

where **m**, **B**, V_m, μ_0, and μ are the magnetic moment, magnetic flux density, volume of magnetic material, magnetic permeability, and magnetic permeability of the material, respectively. In addition, R_c and $\boldsymbol{v_c}$ are the radius and velocity of the colloidosomes, and η and $\boldsymbol{v_{blood}}$ are the viscosity and velocity of blood, respectively. Based on Equations (1) and (2), decreasing the volume of magnetic material within the colloidosomes decreases the magnetic moment, which leads to a reduction in the magnetic force. This indicates that the magnetic force acting on the colloidosomes is inversely proportional to the volume of magnetic Fe$_2$O$_3$

nanoparticles (V_m) [40]. Assuming that the colloidosome is assembled with only one layer of closely arranged CF@PEM-RGD on the surface of a sphere with radius R_c, V_m can be estimated using Equation (5):

$$V_m = \frac{4\pi(R_c + r)^2}{2\sqrt{3}r^2} \times V_b \tag{5}$$

where r is the radius of CF@PEM-RGD, V_b is the volume of the Fe$_2$O$_3$ nanoparticles in an individual CF@PEM-RGD, which can be estimated from the thermogravimetric curve (Fig. S4), and $4\pi(R_c+r)^2/2\sqrt{3}\ r^2$ is the number of CF@PEM-RGD within an individual colloidosome. In brief, the locomotion of colloidosomes in flowing blood and in the

presence of a magnetic field can be described using these equations. Therefore, the net force (F_f) driving colloidosomes toward the magnet highly depends on the radius of the colloidosome and the input magnetic flux density and is inversely proportional to the velocity of blood. Moreover, the $v_{blood}-R_c-F_f$ profile can be theoretically modeled, as shown in Fig. 4I. When a fixed magnetic field is applied, the colloidosome with a larger radius can resist the drag force of blood flowing at a higher velocity, which indicates that a stronger magnetic force acts on a larger colloidosome; therefore, MC colloidosomes outperform CF@PEM-RGD in locomoting upstream. Furthermore, this theoretical model can be used to predict the aspects of colloidosome locomotion.

3.4. Locomotion behavior of MC-CF@PEM-RGD doped with TXA-NH$_3$$^+$ in the presence of a magnetic field

Based on the above-mentioned results, we hypothesized that the magnetic responsiveness and TXA-NH$_3$$^+$-dominated drug release capacity of the colloidosomes can serve as the navigation system and "blast" system to simulate the attack process of torpedoes, thus enabling the microparticles to advance into the deep sites of wounds and accelerate hemostat delivery. As shown in Fig. 5A, the expanding TXA-NH$_3$$^+$ solution (0.5 M, pH 4.5) and external magnetic field provided a sudden propulsion effect that propelled an individual MC-CF@PEM-RGD to move outside the microscope field of vision, leaving a "cloud" within 0.18 s. Furthermore, MC-CF@PEM-RGD doped with TXA-NH$_3$$^+$ (in powder form) was fed at the top of a glass tube (4 mm in diameter and 5.5 cm in length), and the trajectories of the colloidosomes in the top, middle, and bottom parts of the tube were imaged. As shown in Fig. 5C, aggregates of MC-CF@PEM-RGD with an average diameter of 0.38 ± 0.23 mm (Fig. S5) rapidly traveled outside the camera field of vision in the top and middle parts of the tube under magnetic guidance, and the volume of aggregates gradually decreased during locomotion, leaving CO$_2$ bubbles behind. Moreover, the aggregates generated CO$_2$ bubbles for several seconds after reaching the bottom of the tube. This indicates that the external MC-CF@PEM-RGD of the aggregates first disassembled and transformed into capsules through TXA-NH$_3$$^+$ stimulus, and the interior MC-CF@PEM-RGD of the aggregates was temporarily protected until contact with TXA-NH$_3$$^+$ occurred. In contrast, in the absence of a magnetic field, the MC-CF@PEM-RGD aggregates initially traveled toward the bottom because of gravity, as shown in Fig. 5B. However, as the amount of CO$_2$ bubbles increased, the buoyancy generated by the CO$_2$ bubbles surpassed the effect of gravity, leading to a reversal in the motion of the MC-CF@PEM-RGD aggregates. In addition, in the presence of an external magnetic field, the MC-CF@PEM-RGD aggregates arrived at the bottom of the container within 1 s and rapidly spread to the wall of the container (height of 5.5 cm and inner diameter of 4 cm) because of convection and the lateral propulsion of CO$_2$ bubbles (Fig. 5D and Supplementary Movie 8). Based on the above-mentioned results, it can be concluded that hemostat release from MC-CF@PEM-RGD/TH occurred upon contact with water/blood. Nevertheless, the MC-CF@PEM-RGD/TH could reach deep sites with a height of 5.5 cm within 1 s under the actuation of a magnetic field, leading to the release of hemostats at the deep sites. In addition, these results demonstrated the programmed sequential delivery of a hemostat using MC-CF@PEM-RGD, a platform inspired by the action of torpedoes under static conditions (Fig. 5E).

Supplementary video related to this article can be found at https://doi.org/10.1016/j.bioactmat.2022.01.002

To simulate a more realistic condition, the blood flow speed was varied from 0 to 30 mm/s to mimic the physiological flow speed of the post-capillary and arteries after injury, and the maximum displacement of the colloidosomes through the glass tube with and without a magnetic field was determined (Fig. 5F). As shown in Fig. 5G and H, without the application of a magnetic field, MC-CF@PEM-RGD applied at $0°$ opposed blood speeds of up to 5 mm/s, and an increased angle significantly decreased the displacement of MC-CF@PEM-RGD in

flowing blood. This trend indicated that the buoyancy generated by CO$_2$ bubbles facilitated upward locomotion, even in the direction opposite to gravity. However, buoyancy also blocked the downward motion, thus limiting drug diffusion. With the application of a magnetic field, MC-CF@PEM-RGD moved upstream through the entire tube to a maximum distance of 4 cm in all directions when the flow speed was less than 10 mm/s (Fig. 5I and J). In particular, MC-CF@PEM-RGD applied at $180°$ traveled a distance of ~ 2 cm with the assistance of a magnetic field, even when the flow speed increased to 20 mm/s, indicating that the magnetic force determined the locomotion of the colloidosomes, regardless of the direction of buoyancy. According to the mathematical model (Fig. 4I), the larger MC-CF@PEM-RGD aggregates in powder form possessed enhanced magnetic responsiveness, leading to a stronger locomotion capacity against flow. Therefore, a hemostat delivery strategy inspired by torpedoes was achieved by a synergistic combination of magnetic-mediated navigation and TXA-NH$_3$$^+$ stimulation.

3.5. Hemostatic mechanism of MC-CF@PEM-RGD

To clearly illustrate the coagulant mechanism of MC-CF@PEM-RGD, the adhesion of platelets and erythrocytes was first measured. As shown in Fig. 6B, the presence of RGD in both CF@PEM-RGD and MC-CF@PEM-RGD significantly enhanced the aggregation of platelets on the particle surfaces. However, all the particles showed similar erythrocyte adhesion efficiencies. Furthermore, the SEM images (Fig. 6C) confirmed that the activated platelets (fuchsia pseudocolor) with pseudopodium adhered to the surface of MC-CF@PEM-RGD (green pseudocolor). In addition, erythrocytes (orange pseudocolor) also adhered to the surface of the colloidosomes due to electrostatic interactions. To demonstrate that the resultant RGD-PEM capsules could target activated platelets and further accelerate coagulation, CD41a-eFluor 450 and FIIC as markers for activated platelets and capsules, respectively, were used for flow cytometry. The RGD capsules exhibited significantly enhanced interactions with activated platelets, and the binding rate was 2.4 times higher than that of the capsules without modification (Fig. 6D and E). Similarly, the fluorescence images showed that the RGD-PEM capsules (green) and activated platelets (blue) were clearly colocalized, confirming the excellent platelet-aggregating capacity of the RGD-PEM capsules (Fig. 6F). A mixture of MC-CF@PEM-RGD doped with TXA-NH$_3$$^+$ was incubated with plasma (2 × diluted). After 10 min of incubation, a fibrous precipitate composed of platelets and fibrin was formed. Interestingly, the precipitate rapidly moved toward the permanent magnet, indicating that RGD-PEM capsules containing Fe$_2$O$_3$ existed in the fibrin plug (Fig. 6G). In addition, the RGD-PEM capsules and model drug dextran-RBITC released from MC-CF@PEM-RGD were uniformly distributed among the platelet and fibrin aggregates (Fig. 6H), which supported the above-mentioned results.

To further evaluate the platelet-aggregating capacity of the capsules with and without RGD modification under flowing conditions, a microfluidic chamber was used to mimic the dynamic condition of bleeding (Fig. 6I). In brief, FITC-labeled RGD-PEM capsules and CD41a-eFluor 450 labeled resting platelets were injected into the chamber at a flow speed of 5 mm/s. The results indicated that the RGD-PEM capsules had a relatively higher binding efficiency than the capsules without RGD modification (Fig. 6J). The adhesion of the RGD-PEM capsules on the slide was mainly caused by either direct binding between RGD and collagen or the mediation of activated platelets [41]. SEM images also showed that activated platelets with irregular shapes aggregated on the surface of the RGD-PEM capsules (Fig. 6K). Therefore, these *in vitro* experiments under static and dynamic conditions demonstrated that the RGD peptide on the capsule surfaces mediated platelet aggregation. The navigation and "blast" systems of MC-colloidosomes facilitated the diffusion of the RGD-PEM capsules and TH into the cavity of vase-type wounds to activate clotting at the source of bleeding (Fig. 6A).
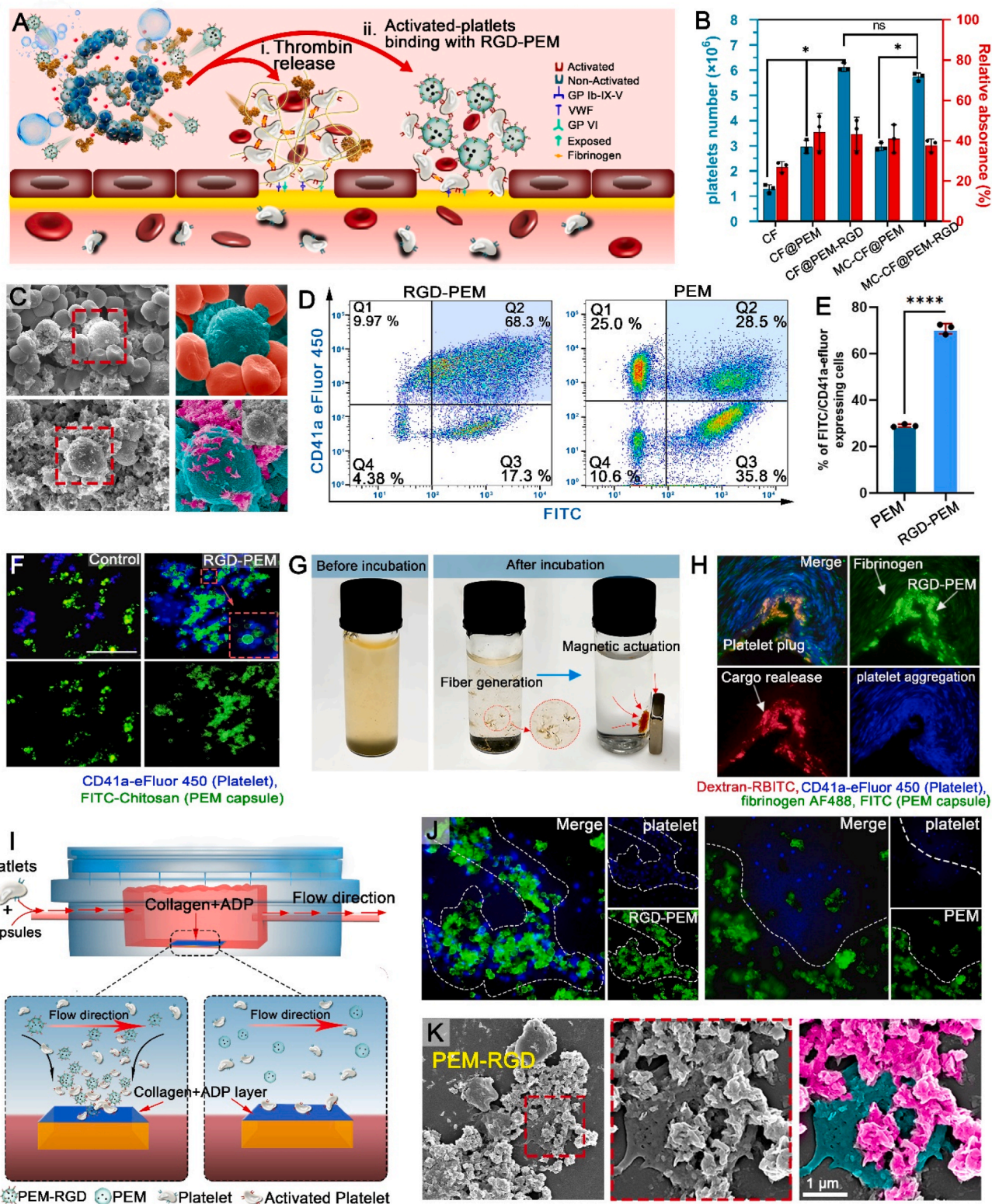
Fig. 6. Hemostatic mechanism of the MC colloidosomes. (**A**) Schematic diagram illustrating the hemostatic mechanism of MC-CF@PEM-RGD/TH. (**B**) Platelet and erythrocyte adhesion on the surface of different particles. (**C**) SEM images illustrating the adhesion of platelets and erythrocyte on surface of MC-CF@PEM-RGD. The red pseudocolor represents erythrocyte, the pink pseudocolor represents the activated platelets, and the green pseudocolor represents RGD-PEM. (**D**) Representative dot plots illustrating the binding rate of activated platelets and RGD-PEM, (**E**) corresponding fluorescence-activated cell sorting analysis, and (**F**) corresponding fluorescence images. (**G**) Photograph of plasma before and after incubation with RGD-PEM and (**H**) corresponding fluorescence images. (**I**) Microfluidic chamber used to assess the binding ability of RGD-PEM under dynamic conditions (10 mm/s). (**J**) Corresponding fluorescence images and (**K**) SEM images. The pink pseudocolor represents the activated platelets, and green pseudocolor represents RGD-PEM.

3.6. Performance of MC-CF@PEM-RGD/TH in vitro complex bleeding model

An *in vitro* bleeding model that mimics the massive bleeding of vase-type wounds (Fig. 7A) was designed in-house. Fresh blood was introduced into the device at different flow speeds (0.5–30 mm/s) controlled by a syringe pump, and the following four groups were selected for further analysis: (I) blank control, (II) MC-CF@PEM-RGD/TH + TXA-NH^{3+}, (III) MC-CF@PEM-RGD/TH with magnetic field, and (IV) MC-CF@PEM-RGD/TH + TXA-NH^{3+} with magnetic field. CF@PEM-RGD-MC/TH in group II facilitated the formation of a clot at the entrance to achieve occlusion at a low blood flow speed (up to 3 mm/s) because the buoyancy of CO_2 bubbles blocked the downward transportation of TH (Fig. 7B). Group III facilitated the formation of an occlusion at flow speeds below 5 mm/s. However, even at a flow speed of 10 mm/s, group IV can facilitate occlusion of the bleeding points within 4 min. Fig. 7C, Supplementary Movie 9, and Fig. S6A depict the entire experimental procedure and spatiotemporal distribution of microparticles by fluorescence microscopy after occlusion (at a flow speed of 5 mm/s). No fluorescence signal was observed in group II, indicating that minimal downward displacement of the microparticles was achieved with gas propulsion. Moreover, without magnetic navigation, most of the TH was released at the top sites of the model and could be easily washed away, particularly by high-speed blood flow. For group III, the fluorescence signal mainly accumulated on the middle three branches at the bottom because of the strong attraction of the magnetic field, leading to rapid sinking without lateral diffusion. However, in group IV, the fluorescence signal was widely distributed at the bottom, and clots formed to occlude all the branches, demonstrating the vital role of magnetic actuation and CO_2 propulsion for vertical transportation and lateral diffusion of the drug. The model was excised and evaluated using SEM to determine the microstructure of the hemostatic clots. As shown in Figs. 7E and S6B, all branches of group IV were filled with a larger number of erythrocytes to form a 3D plug. Furthermore, the high-magnification SEM images of the lateral branch clearly showed that the RGD-PEM capsules were entangled in a high density of erythrocytes. These results demonstrated that the combination of magnetic actuation and gas propulsion synergistically promoted drug convection and diffusion into an inflated cavity, which supported the results of fluorescence microscopy. On the contrary, the clot could only be observed in the middle three branches in group III and was not observed in group II. Therefore, this novel hemostat delivery strategy based on the attack process of torpedoes is a feasible approach for the effective transportation of hemostats into the inflated cavities of vase-neck wounds against blood flow to increase the coagulation effect (Fig. 7D).

Supplementary video related to this article can be found at https://doi.org/10.1016/j.bioactmat.2022.01.002

### 3.7. In vivo hemostasis evaluation

Owing to the outstanding *in vitro* coagulation effect, biocompatibility, and biodegradability of MC-CF@PEM-RGD (Supplementary Description S1, Figs. S7, S8, and S9), we further evaluated its hemostatic performance in rabbit liver models. In particular, a vase-type wound with a small entrance (inner diameter of 4 mm) and a large inner cavity (inner diameter of 10 mm) were made on the liver (Fig. 8A). Subsequently, the wound was subjected to different treatments: (I) gauze, (II) Celox™, (III) MC-CF@PEM-RGD/TH + TXA-NH$_3^+$, (IV) CO-CF@PEM-RGD/TH with magnetic field, (V) MC-CF@PEM-RGD/TH + TXA-NH$_3^+$ with a magnetic field, and (VI) MC-CF@PEM/TH + TXA-NH$_3^+$ with a magnet. Representative photographs of the surgical procedure are shown in Fig. 8B. The vase-type wound was constructed using a No. 12 knife with a crooked tool nose, leading to severe bleeding in the direction opposite to gravity. Different substances were immediately applied to cover the blood holes, and the hemostatic time was recorded. The hemostatic time for the no-treatment group was more than 1000 s, while

that for the gauze and Celox™ groups (Fig. 8C) was approximately 629 $\pm$ 33.7 s and 194 $\pm$ 42 s, respectively. MC-CF@PEM-RGD/TH + TXA-NH$_3^+$ with magnetic field facilitated the shortest coagulation time (75.8 $\pm$ 12.3 s), which was significantly shorter than that for MC-CF@PEM-RGD/TH + TXA-NH$_3^+$ (138.8 $\pm$ 23.0 s) and MC-CF@PEM-RGD/TH with magnetic field (158.2 $\pm$ 25.4 s). This was ascribed to the synergistic effect of magnetic actuation and TXA-NH$_3^+$ stimulation, which facilitated the accelerated transportation of MC-CF@PEM-RGD/TH against blood flow into the injured vasculature. In addition to TH and gas release, the byproducts Ca^{2+} and tranexamic acid can also promote clot formation [42,43]. Notably, even with magnetic actuation and TXA-NH$_3^+$ stimulation, the colloidosomes without RGD modification showed lower hemostatic efficiency than the colloidosomes with RGD modification, demonstrating the vital role of the RGD peptide in accelerating hemostasis.

Furthermore, postoperative analysis of complex wounds was conducted using H&E staining and fluorescence staining. For the Celox™-treated wounds (Fig. 8D), Celox™ was mainly distributed at the top of the wound and did not enter the wound because of its inability to overcome high-pressure bleeding. In contrast, without magnetic field actuation (Figure E-b), FITC-labeled MC-CF@PEM-RGD/TH + TXA-NH$_3^+$ traveled into the middle of the inner cavity, showing a better penetration ability than Celox™ owing to the propulsion effect of CO_2 gas, as demonstrated by Ga et al. (Fig. 8E–e). However, MC-CF@PEM-RGD/TH and the released TH only blocked the top sites of the wound and could not easily reach the deep sites of the inflated cavity, leading to a high pressure in the cavity, which might have destroyed the unstable blood clot on the wound surface and resulted in failed hemostasis. Importantly, with magnetic field actuation (Figure E-a), MC-CF@PEM-RGD/TH (group IV) moved against the blood flow to reach the bottom of the inner cavity. However, the TH within colloidosomes was not released in the absence of pH stimulation (Fig. 8E–d), causing a weaker hemostatic effect than groups III and V. As expected, the histological sections of the wounds treated by group V showed that MC-CF@PEM-RGD/TH was distributed at the bottom of the large inner cavity, which confirmed that the particles moved vertically and laterally with the synergistic effect of magnetic actuation and pH stimulation (Fig. 8E–c). These observations support the results of the *in vitro* bleeding model, further demonstrating that MC-CF@PEM-RGD/TH could be actuated through the vase-neck of wounds against blood flow and could simultaneously accelerate the diffusion of RDG-PEM and TH in the inflated cavity for the clotting of secluded injured vasculature (Fig. 8E–f).

4. Conclusions

Inspired by the attack process of torpedoes, we designed new MC colloidosomes to deliver TH into the deep sites of vase-type wounds using magnetic actuation. Moreover, the burst release of TH and CO_2 bubbles occurred via TXA-NH$_3^+$ stimulation, which promoted the vertical and lateral diffusion of TH and RGD PEM inside the inflated cavity and activated clotting at the source of bleeding. In particular, the magnet-mediated locomotion of individual MC colloidosomes in blood flowing at different velocities was experimentally characterized using an in-house model and theoretically described using a mathematical model. In the rabbit liver trauma model, MC colloidosomes doped with TXA-NH$_3^+$ with magnetic actuation showed the best hemostatic outcome. In addition, cytotoxicity tests, hemolysis assessments, and *in vivo* subcutaneous muscle and liver implantation models indicated that the MC colloidosomes were biocompatible and biodegradable and exerted negligible side effects on healthy tissues (Supplementary Description S1). This study successfully integrated magnetic navigation and gas propulsion into one microplatform for the effective delivery of hemostats into the cavity of vase-type wounds, which may provide new insights for the design of next-generation hemostatic delivery systems to control severe bleeding on the battleground.
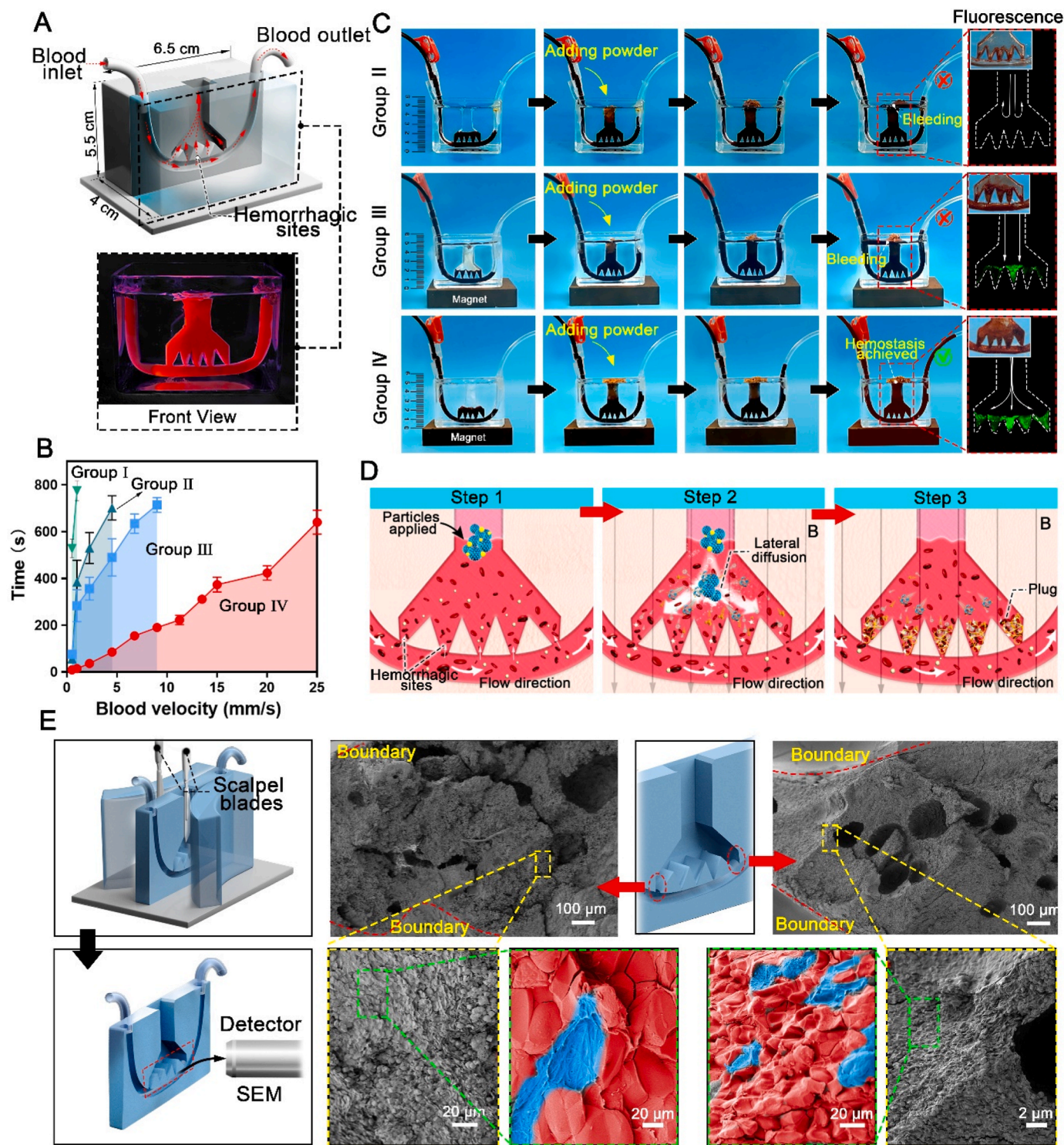
Fig. 7. In vitro evaluations of the MC colloidosomes. (**A**) Schematic diagram and photograph of the *in vitro* bleeding model designed to mimic the massive bleeding originating from inside a vase-type wound. (**B**) Average coagulation time of the different groups using the *in vitro* bleeding model. n = 5 independent samples. (**C**) Representative photographs demonstrating the hemostatic properties of the different groups using the *in vitro* model at a blood flow speed of 5 mm/s and corresponding fluorescence images illustrating the distribution of MC-CF@PEM-RGD. (**D**) Illustration of the mechanism of MC-CF@PEM-RGD/TH combined with TXA-NH_3^+ in the presence of a magnetic field for accelerated coagulation. (**E**) Schematic diagram illustrating the precise excision of a bleeding model using a micro-blade and SEM images of the hemostatic plugs formed in the branches, which were fixed by glutaraldehyde (2.5%). The red pseudocolor represents erythrocytes, and the blue pseudocolor represents RGD-PEM capsules.
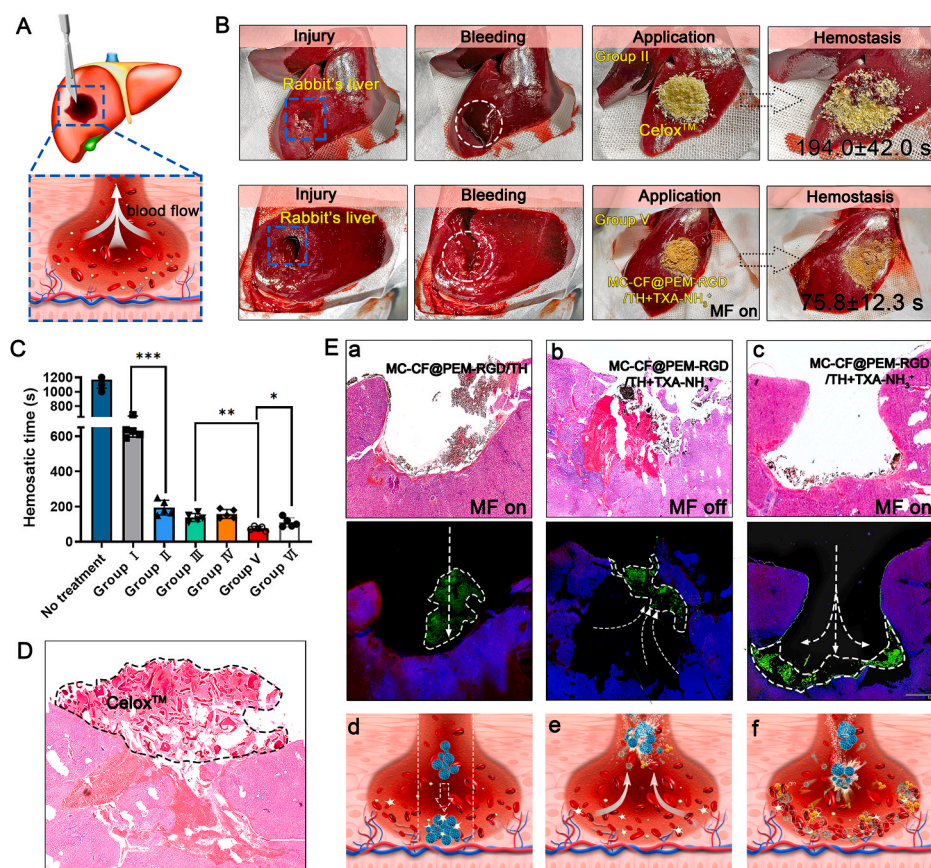
Fig. 8. In vivo evaluations of the MC colloidosomes. (**A**) Schematic diagram illustrating the rabbit liver hemorrhage model with a vase-type wound. (**B**) Representative photographs showing the surgical procedure for groups II and V. (**C**) Average coagulation time achieved by the different groups for the *in vivo* model, n = 3 independent samples, *P < 0.05 **P < 0.01, ***P < 0.001. (**D**) H&E histological sections of wound treated by Celox™. (**E**) Histological sections for H&E staining and fluorescence staining (a–c) and corresponding schematic diagram of hemostasis (d–e).

CRediT authorship contribution statement

Bitao Lu: Investigation, Methodology, Formal analysis, Writing – original draft. **Enling Hu:** Conceptualization, Formal analysis, Writing – review & editing. **Ruiqi Xie:** Data curation. **Kun Yu:** Data curation. **Fei Lu:** Validation. **Rong Bao:** Animal experiments, Formal analysis. **Chenhui Wang:** Funding acquisition. **Guangqian Lan:** Supervision, of all aspects of this work. **Fangyin Dai:** Supervision, of all aspects of this work.

Declaration of competing interest

We declare that we have no financial and personal relationships with other people or organizations that can in appropriately influence our work, there is no professional or other personal interest of any nature or kind in any product, service and/or company that could be construed as influencing the position presented in, or the review of, the manuscript entitled "Microcluster bomb-like colloidosomes for hemostat delivery into vase-type wounds: a platform inspired by the attack action of torpedoes".

Acknowledgments

Appendix A. Supplementary data

Supplementary data to this article can be found online at https://doi.org/10.1016/j.bioactmat.2022.01.002.

References

[1] Y. Huang, X. Zhao, Z. Zhang, Y. Liang, Z. Yin, B. Chen, et al., Degradable gelatin-based IPN cryogel hemostat for rapidly stopping deep noncompressible hemorrhage and simultaneously improving wound healing, Chem. Mater. 32 (2020) 6595–6610.

[2] B.J. Eastridge, R.L. Mabry, P. Seguin, J. Cantrell, T. Tops, P. Uribe, et al., Death on the battlefield (2001-2011): implications for the future of combat casualty care, Journal of Trauma and Acute Care Surgery 73 (2012) S431–S437.

[3] D.R. King, Initial care of the severely injured patient, N. Engl. J. Med. 380 (2019) 763–770.

[4] M.A. Khan, M. Mujahid, A review on recent advances in chitosan based composite for hemostatic dressings, Int. J. Biol. Macromol. 124 (2019) 138–147.

[5] J. Jin, Z. Ji, M. Xu, C. Liu, X. Ye, W. Zhang, et al., Microspheres of carboxymethyl chitosan, sodium alginate, and collagen as a hemostatic agent in vivo, ACS Biomater. Sci. Eng. 4 (2018) 2541–2551.

[6] H. Yuan, L. Chen, F.F. Hong, A biodegradable antibacterial nanocomposite based on oxidized bacterial nanocellulose for rapid hemostasis and wound healing, ACS Appl. Mater. Interfaces 12 (2020) 3382–3392.

[7] Y. Liang, C. Xu, F. Liu, S. Du, G. Li, X. Wang, Eliminating heat injury of zeolite in hemostasis via thermal conductivity of graphene sponge, ACS Appl. Mater. Interfaces 11 (2019) 23848–23857.

[8] Q. Li, E. Hu, K. Yu, R. Xie, F. Lu, B. Lu, et al., Self-propelling janus particles for hemostasis in perforating and irregular wounds with massive hemorrhage, Adv. Funct. Mater. 30 (2020).

[9] Y. Liang, X. Zhao, T. Hu, B. Chen, Z. Yin, P.X. Ma, et al., Adhesive hemostatic conducting injectable composite hydrogels with sustained drug release and photothermal antibacterial activity to promote full-thickness skin regeneration during wound healing, Small 15 (2019), 1900046.

[10] S. Mansor, A. Aldiasy, A. Algialany, A. Buzaja, The operative management for gunshot liver injuries: an experience of seventy-one patients in 5 years, Indian J. Surg. 83 (1) (2021) 149–154.

[11] N. Christmas, A.U. Vakil, C.J. Hatch, S. Dong, D. Fikhman, H.T. Beaman, et al., Characterization of shape memory polymer foam hemostats in in vitro

hemorrhagic wound models, J. Biomed. Mater. Res. B Appl. Biomater. 109 (2021) 681–692.

[12] R. Abaza, K. Lukens-Bull, L. Bayouth, C. Smotherman, J. Tepas, M. Crandall, Gunshot wound incidence as a persistent, tragic symptom of area deprivation, Surgery 168 (2020) 671–675.

[13] L. Yao, H. Gao, Z. Lin, Q. Dai, S. Zhu, S. Li, et al., A shape memory and antibacterial cryogel with rapid hemostasis for noncompressible hemorrhage and wound healing, Chem. Eng. J. 428 (2022), 131005.

[14] H. Wang, Z. Zhao, Y. Liu, C. Shao, F. Bian, Y. Zhao, Biomimetic enzyme cascade reaction system in microfluidic electrospray microcapsules, Sci. Adv. 4 (2018), eaat2816.

[15] Q. Li, F. Lu, S. Shang, H. Ye, K. Yu, B. Lu, et al., Biodegradable microporous starch with assembled thrombin for rapid induction of hemostasis, ACS Sustain. Chem. Eng. 7 (2019) 9121–9132.

[16] L. Hui, K.M. Wang, Torpedo performance Markov model, Expert Syst. Appl. 42 (2015) 9129–9136.

[17] W. Wang, Z. Wu, X. Lin, T. Si, Q. He, Gold-nanoshell-functionalized polymer nanoswimmer for photomechanical poration of single-cell membrane, J. Am. Chem. Soc. 141 (2019) 6601–6608.

[18] L. Xie, X. Pang, X. Yan, Q. Dai, H. Lin, J. Ye, et al., Photoacoustic imaging-trackable magnetic microswimmers for pathogenic bacterial infection treatment, ACS Nano 14 (2020) 2880–2893.

[19] L. Chen, S.-F. Zhou, L. Su, J. Song, Gas-mediated cancer bioimaging and therapy, ACS Nano 13 (2019) 10887–10917.

[20] V. Magdanz, I.S.M. Khalil, J. Simmchen, G.P. Furtado, S. Mohanty, J. Gebauer, et al., IRONSperm: sperm-templated soft magnetic microrobots, Sci. Adv. 6 (2020). No. eaba5855.

[21] M. Fernández-Medina, M.A. Ramos-Docampo, O. Hovorka, V. Salgueiriño, B. Städler, Recent advances in Nano- and micromotors, Adv. Funct. Mater. 30 (2020), 1908283.

[22] Y. Alapan, U. Bozuyuk, P. Erkoc, A.C. Karacakol, M. Sitti, Multifunctional surface microrollers for targeted cargo delivery in physiological blood flow, Science Robotics 5 (2020). No. eaba5726.

[23] H. Xu, M. Medina-Sanchez, M.F. Maitz, C. Werner, O.G. Schmidt, Sperm micromotors for cargo delivery through flowing blood, ACS Nano 14 (2020) 2982–2993.

[24] L. Yu, P. Hu, Y. Chen, Gas-generating nanoplatforms: material chemistry, multifunctionality, and gas therapy, Adv. Mater. 30 (2018), 1801964.

[25] J.R. Baylis, J.H. Yeon, M.H. Thomson, A. Kazerooni, X. Wang, A.E. St John, et al., Self-propelled particles that transport cargo through flowing blood and halt hemorrhage, Sci. Adv. 1 (2015), e1500379.

[26] B. van der Kroon, R. Brouwer, P.J.H. van Beukering, The energy ladder: theoretical myth or empirical truth? Results from a meta-analysis, Renew. Sustain. Energy Rev. 20 (2013) 504–513.

[27] Z. Shi, G. Lan, E. Hu, F. Lu, P. Qian, J. Liu, et al., Puff pastry-like chitosan/konjac glucomannan matrix with thrombin-occupied microporous starch particles as a composite for hemostasis, Carbohydr. Polym. (2020) 232.

[28] C. Feng, J. Li, G.S. Wu, Y.Z. Mu, M. Kong, C.Q. Jiang, et al., Chitosan-coated diatom silica as hemostatic agent for hemorrhage control, ACS Appl. Mater. Interfaces 8 (2016) 34234–34243.

[29] Y.S. Gao, A. Sarode, N. Kokoroskos, A. Ukidve, Z.M. Zhao, S.H. Guo, et al., A polymer-based systemic hemostatic agent, Sci. Adv. 6 (2020) 12.

[30] Y. Xu, Y. Gu, F. Cai, K. Xi, T. Xin, J. Tang, et al., Metabolism balance regulation via antagonist-functionalized injectable microsphere for nucleus pulposus regeneration, Adv. Funct. Mater. 30 (2020).

[31] L. Wang, Y. Zhong, C. Qian, D. Yang, J. Nie, G. Ma, A natural polymer-based porous sponge with capillary-mimicking microchannels for rapid hemostasis, Acta Biomater. 114 (2020) 193–205.

[32] Q. Li, F. Lu, S.M. Shang, H.L. Ye, K. Yu, B.T. Lu, et al., Biodegradable microporous starch with assembled thrombin for rapid induction of hemostasis, ACS Sustain. Chem. Eng. 7 (2019) 9121–9132.

[33] Y. He, J. Xu, X. Sun, X. Ren, A. Maharjan, P. York, et al., Cuboidal tethered cyclodextrin frameworks tailored for hemostasis and injured vessel targeting, Theranostics 9 (2019) 2489–2504.

[34] T. Guo, T. Meng, G. Yang, Y. Wang, R. Su, S. Zhou, Dynamic hybrid colloidosomes via electrostatic interactions for pH-balanced low premature leakage and ultrafast cargo release, Nano Lett. 19 (2019) 6065–6071.

[35] S. Zhu, Q. Meng, L. Wang, J. Zhang, Y. Song, H. Jin, et al., Highly photoluminescent carbon dots for multicolor patterning, sensors, and bioimaging, Angew. Chem. Int. Ed. 52 (2013) 3953–3957.

[36] W. Zhou, G. Tong, D. Wang, B. Zhu, Y. Ren, M. Butler, et al., Toward scalable fabrication of hierarchical silica capsules with integrated micro-, meso-, and macropores, Small 12 (2016) 1797–1805.

[37] W. Wei, Z. Wang, Investigation of magnetic nanoparticle motion under a gradient magnetic field by an electromagnet, J. Nanomater. (2018), 6246917, 2018.

[38] O. Yasa, P. Erkoc, Y. Alapan, M. Sitti, Microalga-powered microswimmers toward active cargo delivery, Adv. Mater. 30 (2018), 1804130.

[39] A. Elbourne, S. Cheeseman, P. Atkin, N.P. Truong, N. Syed, A. Zavabeti, et al., Antibacterial liquid metals: biofilm treatment via magnetic activation, ACS Nano 14 (2020) 802–817.

[40] X. Wang, J. Law, M. Luo, Z. Gong, J. Yu, W. Tang, et al., Magnetic measurement and stimulation of cellular and intracellular structures, ACS Nano 14 (2020) 3805–3821.

[41] F. Zhang, Y. Liu, J. Lei, S. Wang, X. Ji, H. Liu, et al., Metal–organic-framework-derived carbon nanostructures for site-specific dual-modality photothermal/photodynamic thrombus therapy, Adv. Sci. 6 (2019), 1901378.

[42] F. Massimo, M. Pier Mannuccio, The never ending success story of tranexamic acid in acquired bleeding, Haematologica 105 (2020) 1201–1205.

[43] L. Tan, X. Zhou, K. Wu, D. Yang, Y. Jiao, C. Zhou, Tannic acid/CaII anchored on the surface of chitin nanofiber sponge by layer-by-layer deposition: integrating effective antibacterial and hemostatic performance, Int. J. Biol. Macromol. 159 (2020) 304–315.